



## Article

# Encapsulating Metal-Organic-Framework Derived Nanocages into a Microcapsule for Shuttle Effect-Suppressive Lithium-Sulfur Batteries

Jinyun Liu <sup>1,\*</sup>, Yajun Zhu <sup>1,†</sup>, Junfei Cai <sup>2,†</sup>, Yan Zhong <sup>1</sup>, Tianli Han <sup>1</sup>, Zhonghua Chen <sup>3,\*</sup> and Jinjin Li <sup>2,\*</sup>

<sup>1</sup> Anhui Provincial Engineering Laboratory for New-Energy Vehicle Battery Energy-Storage Materials, College of Chemistry and Materials Science, Anhui Normal University, Wuhu 241002, China; yjzhu@ahnu.edu.cn (Y.Z.); yanzhong@ahnu.edu.cn (Y.Z.); hantianli@ahnu.edu.cn (T.H.)

<sup>2</sup> National Key Laboratory of Science and Technology on Micro/Nano Fabrication, Department of Micro/Nano-Electronics, Shanghai Jiao Tong University, Shanghai 200240, China; caijf001@sjtu.edu.cn

<sup>3</sup> Shenzhen FBTech Electronics Ltd., Shenzhen 518100, China

\* Correspondence: jyliu@ahnu.edu.cn (J.L.); chenzhonghua@fbwtt.com (Z.C.); lijijin@sjtu.edu.cn (J.L.)

† These authors contributed equally to this work.

**Abstract:** Long-term stable secondary batteries are highly required. Here, we report a unique microcapsule encapsulated with metal organic frameworks (MOFs)-derived  $\text{Co}_3\text{O}_4$  nanocages for a Li-S battery, which displays good lithium-storage properties. ZIF-67 dodecahedra are prepared at room temperature then converted to porous  $\text{Co}_3\text{O}_4$  nanocages, which are infilled into microcapsules through a microfluidic technique. After loading sulfur, the  $\text{Co}_3\text{O}_4$ /S-infilled microcapsules are obtained, which display a specific capacity of  $935 \text{ mAh g}^{-1}$  after 200 cycles at 0.5C in Li-S batteries. A Coulombic efficiency of about 100% is achieved. The constructed Li-S battery possesses a high rate-performance during three rounds of cycling. Moreover, stable performance is verified under both high and low temperatures of  $50^\circ\text{C}$  and  $-10^\circ\text{C}$ . Density functional theory calculations show that the  $\text{Co}_3\text{O}_4$  dodecahedra display large binding energies with polysulfides, which are able to suppress shuttle effect of polysulfides and enable a stable electrochemical performance.

**Keywords:** secondary battery; nanocomposite; microcapsule; capacity; stability



**Citation:** Liu, J.; Zhu, Y.; Cai, J.; Zhong, Y.; Han, T.; Chen, Z.; Li, J. Encapsulating Metal-Organic-Framework Derived Nanocages into a Microcapsule for Shuttle Effect-Suppressive Lithium-Sulfur Batteries. *Nanomaterials* **2022**, *12*, 236. <https://doi.org/10.3390/nano12020236>

Academic Editor: Christophe Detavernier

Received: 27 November 2021

Accepted: 10 January 2022

Published: 12 January 2022

**Publisher's Note:** MDPI stays neutral with regard to jurisdictional claims in published maps and institutional affiliations.



**Copyright:** © 2022 by the authors. Licensee MDPI, Basel, Switzerland. This article is an open access article distributed under the terms and conditions of the Creative Commons Attribution (CC BY) license (<https://creativecommons.org/licenses/by/4.0/>).

## 1. Introduction

Recently, the demands for electric vehicles and portable electronics have been rapidly increasing. Considering this, investigations on secondary batteries are considered to be a significant direction. People are expecting higher capacity, longer cycling life, and faster charging of secondary batteries. As a promising next-generation secondary battery, the Li-S battery possesses a high theoretical energy density ( $2600 \text{ Wh kg}^{-1}$ ) and low cost of sulfur [1–4]. Recently, the research on Li-S batteries has been considered to be a significant field [5,6]. There are many problems for currently available Li-S batteries, such as the volumetric change of sulfur and shuttle effect reducing the electrochemical performance, which represent obstacles to commercialization [7].

In order to address those issues, many studies have been reported, in which the synthesis of yolk-shell structure hosts is considered to be a potential strategy [8–10]. Zhang et al. reported a yolk-shell ZnO by using a hydrothermal method, which provided a specific capacity of  $1406 \text{ mAh g}^{-1}$  at 0.1C [11]. Jiang et al. synthesized a yolk-shell nanomaterial consisting of  $\text{SiO}_2$  core and carbon shell [12]. The cathode based on the yolk-shell  $\text{SiO}_2$ -carbon delivered  $1200 \text{ mAh g}^{-1}$  at a rate of 0.2C. Those achievements indicate that several yolk-shell structures exhibit enhanced adsorption towards polysulfides [13,14]. Reasonable engineering yolk-shell structure as sulfur host could promisingly improve the energy-storage properties [15,16]. However, general and simple preparation approaches for large-

scale yolk-shell materials are still highly required. In addition, several reports indicated that typical semiconductor  $\text{Co}_3\text{O}_4$  is a promising sulfur host because of its strong interaction with sulfur and polysulfides [17–20]. With this in mind, developing creative  $\text{Co}_3\text{O}_4$ -based composite for Li-S batteries is attractive and would be of great significance [21–23].

Here, we present a microcapsule infilling by a metal–organic framework (MOF)-derived cobalt oxide nanocage as the sulfur host, which displays a high electrochemical performance. By using ZIF-67 as a precursor which was prepared through a hydrothermal approach, a porous dodecahedral  $\text{Co}_3\text{O}_4$  nanocage was obtained (Figure 1). The experimental procedures are presented in the Supplementary Material. Then,  $\text{Co}_3\text{O}_4$  nanocages were encapsulated into microcapsules through a microfluidic strategy. The real-time process of the cone and the formation of drops are displayed by Movie S1 and S2, respectively. The prepared microcapsules were carbonized for use as a sulfur host, which showed a long life of 200 cycles, along with a stable specific capacity of  $935 \text{ mAh g}^{-1}$  and a 100% Coulombic efficiency. After repeated tests, it displays a stable rate-performance, and the battery remains stable at  $-10 \text{ }^\circ\text{C}$  and  $50 \text{ }^\circ\text{C}$ . Furthermore, density functional theory (DFT) calculations show that  $\text{Co}_3\text{O}_4$  possesses large binding energies towards polysulfides, which are important for reducing the shuttle effect and enabling a stable electrochemical performance.

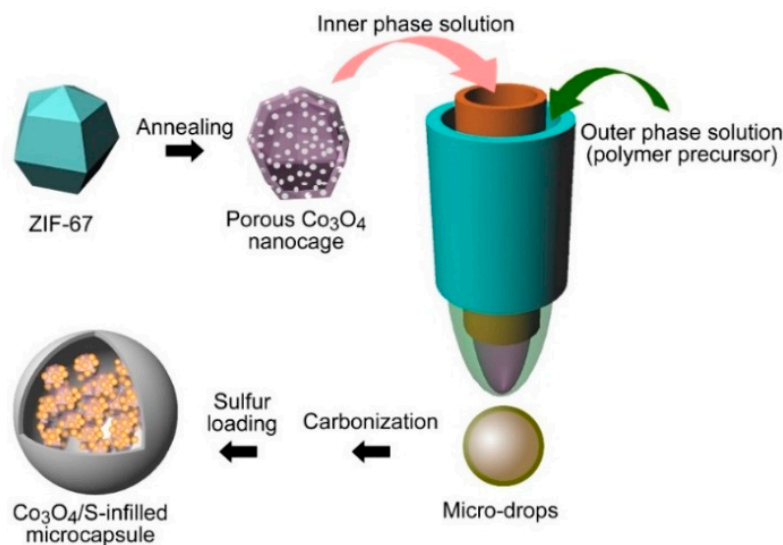


**Figure 1.** Microfluidic preparation of  $\text{Co}_3\text{O}_4$ /S-infilled microcapsules.

## 2. Results and Discussion

### 2.1. Structural and Microstructural Characterization

SEM image (Figure 2a) of ZIF-67 precursor shows a dodecahedron morphology with a size of 500 nm. Figure 2b shows the SEM image of porous dodecahedral  $\text{Co}_3\text{O}_4$  obtained after annealing the precursor. The TEM image (Figure 2c) displays the porous  $\text{Co}_3\text{O}_4$  nanocage clearly. The dodecahedral  $\text{Co}_3\text{O}_4$  was encapsulated in microcapsule by using a coaxial focusing method. Figure 2d shows the SEM image of microcapsules with a size of about  $50 \mu\text{m}$ . The microcapsule was observed by using an optical microscope (Figure 2e), and it is verified the  $\text{Co}_3\text{O}_4$  uniformly distributes in the microcapsule. An SEM image of  $\text{Co}_3\text{O}_4$ -infilled microcapsules after annealing is shown in Figure 2f. A TEM image (Figure 2g) presents the edge of the microcapsule. It is observed that the shell of the microcapsule is very thin after calcination. After the microcapsules were broken manually, dodecahedral  $\text{Co}_3\text{O}_4$  nanocages inside the microcapsule were observed clearly in Figure 2h,i. Figure 2j displays the microcapsules after loading sulfur, forming a  $\text{Co}_3\text{O}_4$ /S-infilled microcapsule structure. The surface become rough, which indicates that some of the sulfur was coated on microcapsules.

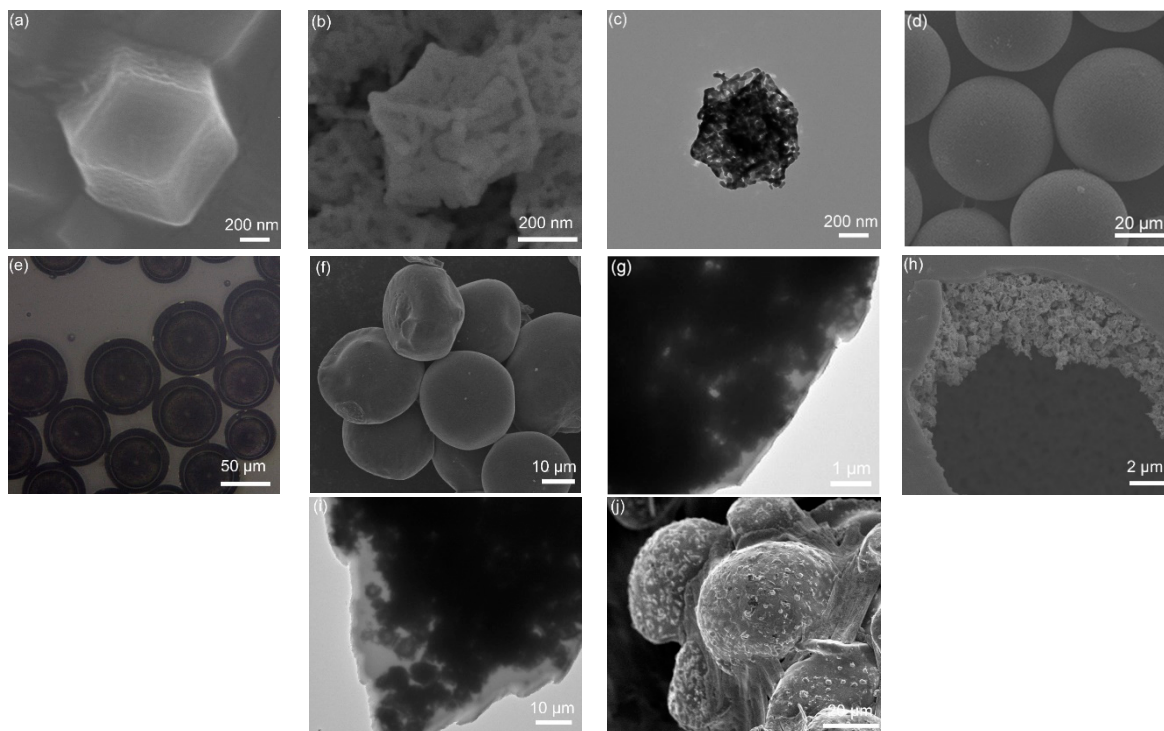


**Figure 2.** SEM photographs of (a) ZIF-67 and (b) dodecahedral  $\text{Co}_3\text{O}_4$  nanocage. (c) TEM image of  $\text{Co}_3\text{O}_4$ . (d) SEM and (e) optical photographs of  $\text{Co}_3\text{O}_4$ -infilled microcapsules before carbonization. (f) SEM and (g) TEM images of carbonized microcapsules. (h) SEM and (i) TEM photographs of  $\text{Co}_3\text{O}_4$ -infilled microcapsule after breaking manually. (j) SEM image of microcapsules after loading sulfur.

The XRD pattern (Figure 3) is assigned to  $\text{Co}_3\text{O}_4$  in terms of JCPDS card No. 42-1467, while the other peaks are attributed to sulfur (JCPDS card No. 99-0066). The signal of  $\text{Co}_3\text{O}_4$  becomes unobvious after loading sulfur, which would be ascribed to the cover of sulfur signals. Figure S1 displays the HRTEM image of the porous  $\text{Co}_3\text{O}_4$ . The  $\text{Co}_3\text{O}_4$  obtained after annealing ZIF-67 precursor exhibits a good crystallinity. The 0.28 nm lattice spacing matches the (220) crystalline plane, while the SAED pattern displays several diffraction rings, indicating a polycrystalline structure [24].

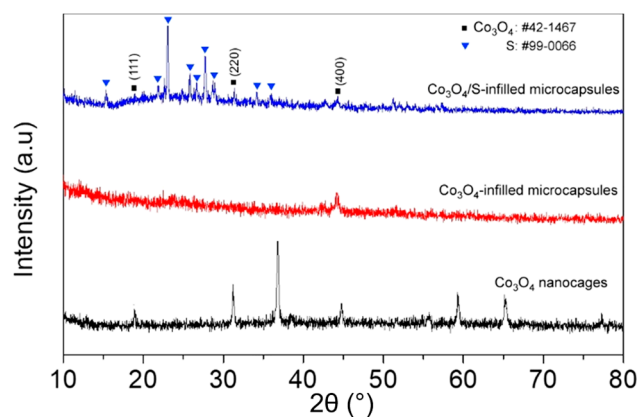


**Figure 3.** XRD patterns of the pristine  $\text{Co}_3\text{O}_4$  nanocages and the capsules infilled with  $\text{Co}_3\text{O}_4$  or  $\text{Co}_3\text{O}_4/\text{S}$  composite.

The composition and chemical states of the microcapsules are presented in the XPS spectra (Figure 4). The peak at 285 eV is from C1s, and the ones at 530 and 790 eV are ascribed to the O1s and Co2p, respectively, as shown in Figure 4a. The C 1s spectrum

(Figure 4b) shows two peaks, where the one at 284.6 eV is indexed to graphite carbon. Moreover, peak at 285.9 eV represents C=O [17]. O 1s spectrum (Figure 4c) exhibits three peaks at 530 eV, 532.2, and 533.5 eV, corresponding to lattice oxygen, -OH and H<sub>2</sub>O molecules, respectively [25–27]. The Co 2P spectrum (Figure 4d) shows 781.0 and 799 eV of Co<sup>2+</sup> [28], and 778.7 and 796.6 eV peaks are from Co<sup>3+</sup> [29,30].

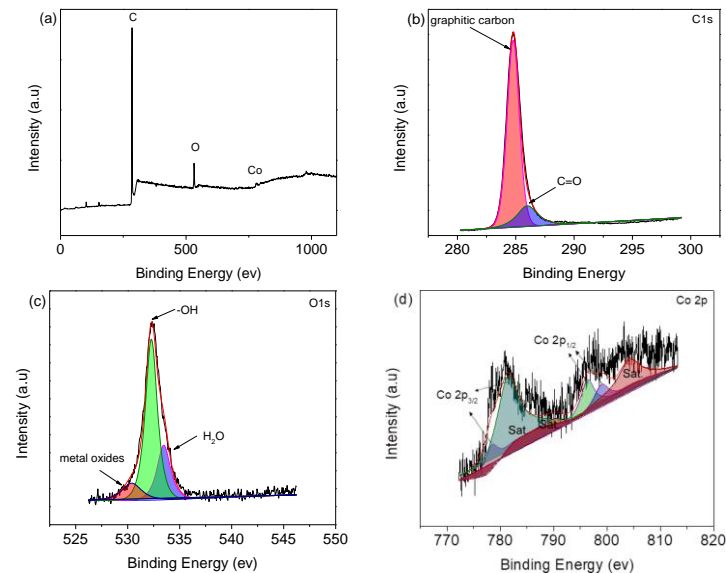


**Figure 4.** (a) XPS survey spectrum of Co<sub>3</sub>O<sub>4</sub>-infilled microcapsules. XPS spectra of (b) C 1s, (c) O 1s, and (d) Co 2p.

The elemental distribution of Co<sub>3</sub>O<sub>4</sub>-infilled microcapsules is shown in Figure 5. The elements C, Co, and O evenly distribute. In Figure 5e, the EDS spectrum shows that the composition of Co<sub>3</sub>O<sub>4</sub> includes C, Co, and O [31], which has a high purity. Figure 6a presents the TGA curves of Co<sub>3</sub>O<sub>4</sub>-infilled microcapsules measured in air. The mass loss from 350 °C to 480 °C is caused by the decomposition of the carbon shell. The drop from 250 to 350 °C is attributed to sulfur evaporation [32,33]. The sulfur in the microcapsules is about 85 wt%, which is significant for a high-sulfur loading. Moreover, pure Co<sub>3</sub>O<sub>4</sub>-infilled microcapsules show that the content of Co<sub>3</sub>O<sub>4</sub> nanocages is about 35 wt%. Figure 6b shows the Raman spectra of the Co<sub>3</sub>O<sub>4</sub>-infilled microcapsules with and without loading sulfur. The D- and G-bands of carbon locate at 1370 and 1670 cm<sup>-1</sup>, respectively. In sulfur-loaded microcapsules, the peaks ranging from 150 to 475 cm<sup>-1</sup> are assigned to sulfur.

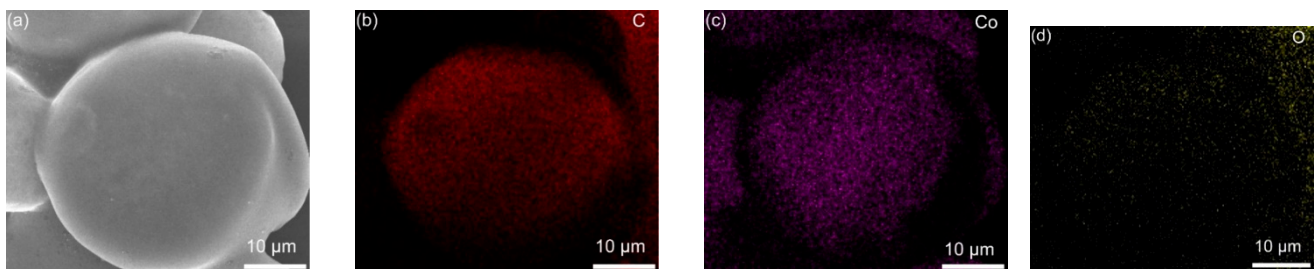


**Figure 5.** (a) SEM and (b–d) mapping images of the Co<sub>3</sub>O<sub>4</sub>-infilled microcapsules. (e) Related EDS spectrum.

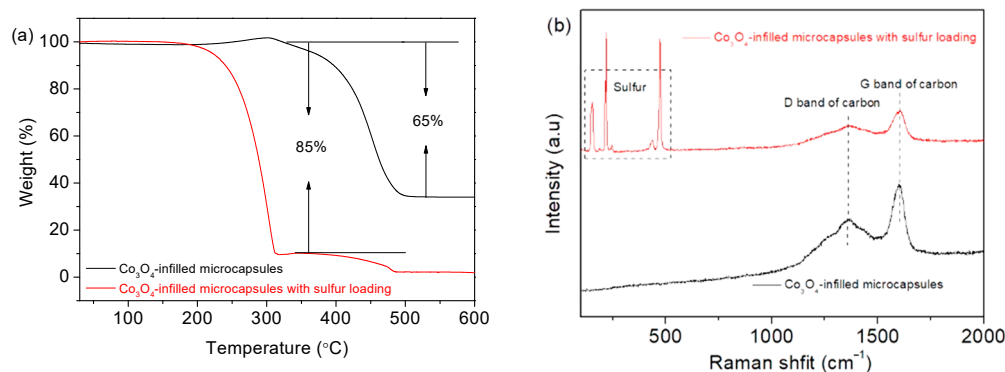


**Figure 6.** (a) TGA profiles and (b) Raman spectra of Co<sub>3</sub>O<sub>4</sub>-infilled microcapsules with and without loading sulfur.

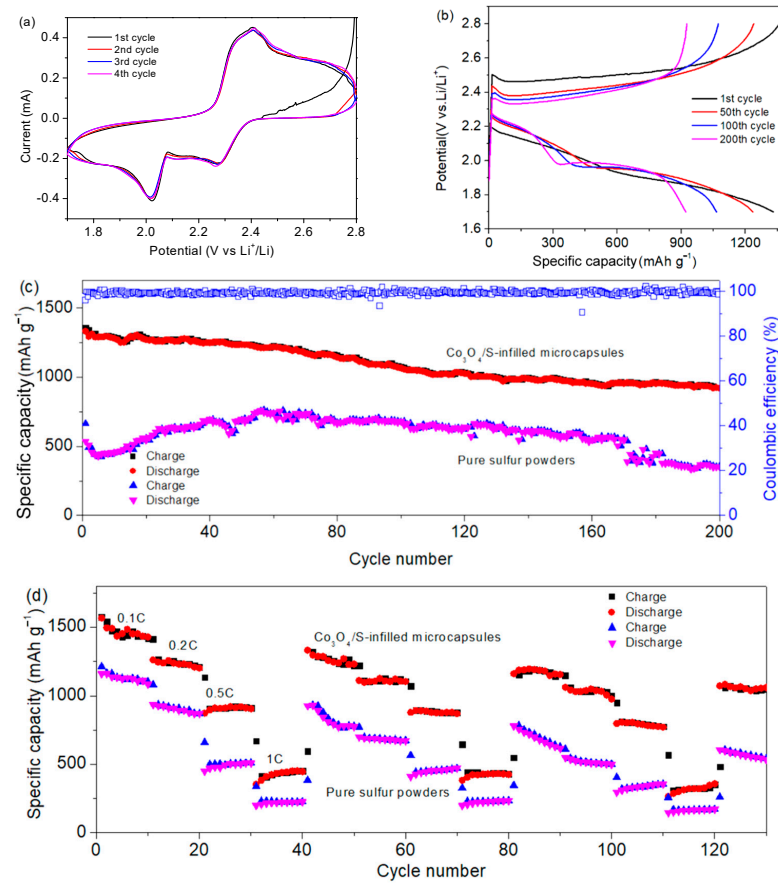
## 2.2. Electrochemical Characterization

Figure 7a displays the CV curves. During the discharge, two reduction peaks at 2.25 and 1.95 V are attributed to the conversion of high-order polysulfide to Li<sub>2</sub>S<sub>4</sub> and reduction of Li<sub>2</sub>S<sub>4</sub> to Li<sub>2</sub>S<sub>2</sub>/Li<sub>2</sub>S [34,35]. In the charging process, the oxidation at 2.4 V is ascribed to the conversion of Li<sub>2</sub>S<sub>2</sub>/Li<sub>2</sub>S to Li<sub>2</sub>S<sub>n</sub> [36]. In Figure 7b, two discharge plateaus at 2.2 and 1.9 V are verified. The platform at 2.4 V in charge corresponds to oxidation peak [37]. It is noted that the overpotentials are observed, which may be attributed to the non-completed carbonization and the resulting limited conductivity. Figure 7c shows that the specific capacity remains 935 mAh g<sup>-1</sup> after cycling 200 times at 0.5C (1C equates to fully charging or discharging the theoretical capacity in 1 h). The Coulombic efficiency is close to 100%. Compared to the performance of the Co<sub>3</sub>O<sub>4</sub>/S-infilled microcapsules, the capacity of pure sulfur powders is very low. In particular, the capacity decays rapidly after 150 cycles. In addition, the electrochemical performance of the microcapsules is also competitive compared to some other composites, as displayed in Table 1. Figure 7d shows the rate performance after repeated tests. In the second round, specific capacities are 1250, 1150, 860, and 500 mAh g<sup>-1</sup> at rates of 0.1C, 0.2C, 0.5C, and 1C, respectively. It recovers to 1190 mAh g<sup>-1</sup> once the rate is returned to 0.1C. Microcapsules exhibit a better reversibility and higher capacities than sulfur powders. It is attributed to the improved conductivity by the carbon shell and the reduced polysulfide loss by Co<sub>3</sub>O<sub>4</sub> adsorption, which will be demonstrated by DFT calculations.

The Co<sub>3</sub>O<sub>4</sub>/S-infilled microcapsules-based Li-S battery also displays good cycling stability under different temperatures. Figure 8a shows that the capacity remains at 647 mAh g<sup>-1</sup> after cycling 200 times under -10 °C. Besides cycling at a low temperature, the electrochemical performance at 50 °C is presented in Figure 8b, showing a specific capacity of 713 mAh g<sup>-1</sup> after 200 cycles. Stable performance indicates that microcapsules can be used in different conditions, which are significant for practical applications.

Figure 9a displays CV curves of Co<sub>3</sub>O<sub>4</sub>/S-infilled microcapsules at 0.6 to 1 mV s<sup>-1</sup>; Figure 9b displays a logarithmic relationship according to  $i = av^b$ , where  $i$  and  $v$  stand for the peak current and rate, respectively [49]. The  $b$  value of 0.5 represents a diffusive-controlled process, and  $b = 1$  indicates a capacitive behavior. In this investigation,  $b$  values suggest mainly diffusion-controlled processes. Figure 9c shows the diffusion contribution ratios calculated on the basis of  $i(v) = k_1v + k_2v^{1/2}$ , where  $k_1v$  and  $k_2v^{1/2}$  stand for capacitive and diffusion-controlled contributions, respectively. The results were fitted (Figure 9d) based on  $I_p = 2.69 \times 10^5 \times n^{3/2}AD^{1/2}Cv^{1/2}$  [50], where  $I_p$  is the peak current;  $n$  is the number of electrons transferred during the reaction, which is 2 for Li-S batteries;  $A$  is the active electrode area (1.13 cm<sup>2</sup>);  $D$  is the diffusion coefficient of lithium ion in unit of cm<sup>2</sup> s<sup>-1</sup>;  $C$  is the concentration of Li ions in electrolyte in unit of mol mL<sup>-1</sup> [51,52]; and  $v$  is the scanning rate in the unit of V s<sup>-1</sup>. On the basis of the obtained slopes, the Li ion diffusion coefficients are calculated to be  $3.8 \times 10^{-9}$  and  $1.8 \times 10^{-9}$  cm<sup>2</sup> s<sup>-1</sup>, which are close to some reports [53,54]. The good diffusion property is ascribed to the specific microcapsule

structure, which enables a good environment for contact with electrolytes; the porous scaffold of  $\text{Co}_3\text{O}_4$  nanocages assembled by nanoparticles shortens the transfer pathway of ions.



**Figure 7.** (a) CV curves of  $\text{Co}_3\text{O}_4/\text{S}$ -infilled microcapsules-based Li-S battery scanning at a rate of  $0.1 \text{ mV s}^{-1}$ . (b) Cycling curves at  $0.5\text{C}$ . (c) Cycling performance at a rate of  $0.5\text{C}$ . (d) Rate-performance of different samples.

**Table 1.** Comparison on the electrochemical performance of some composite-based cathodes.

Composite	Preparation Method	Cycling Rate	Cycle Number	Specific Capacity ( $\text{mAh g}^{-1}$ )	Ref.
$\text{TiO}_2@\text{Co}_3\text{O}_4/\text{S}$ nanospheres	Water bath	0.1C	100	817	[38]
$\text{Co}_3\text{O}_4$ powders/S	Hydrothermal method	0.1C	100	706	[39]
$\text{Co}_3\text{O}_4-\text{CoN}/\text{CC}$	Hydrothermal method	3C	500	627	[40]
$\text{Co}_3\text{O}_4/\text{CoO}/\text{GNS}/\text{h-BN}/\text{S}$	Ball-milling	1C	250	356	[41]
$\text{S}@\text{Co}_3\text{O}_4/\text{C}$	Hydrothermal method	1C	500	520	[42]
Nano S/rGO	High pressure steam	5C	100	639	[43]
$\text{NiCo}_2\text{S}_4@\text{S}$	Hydrotherma method	0.5C	500	836	[44]
Yttria hollow spheres@C/S	Hydrothermal method	0.5C	200	842	[45]
$\text{Mo}@\text{N-G}/\text{S}$	Hydrothermal method	1C	500	615	[46]
$\text{S}@\text{N-Ta}_2\text{O}_5/\text{rGO}$	Co-precipitation	2C	600	825	[47]
$\text{S}@\text{MnO}_2@\text{SnO}_2$	Hydrothermal method	0.5C	500	566	[48]
$\text{Co}_3\text{O}_4/\text{S}$ -infilled microcapsules	Microfluidic approach	0.5C	200	935	This work

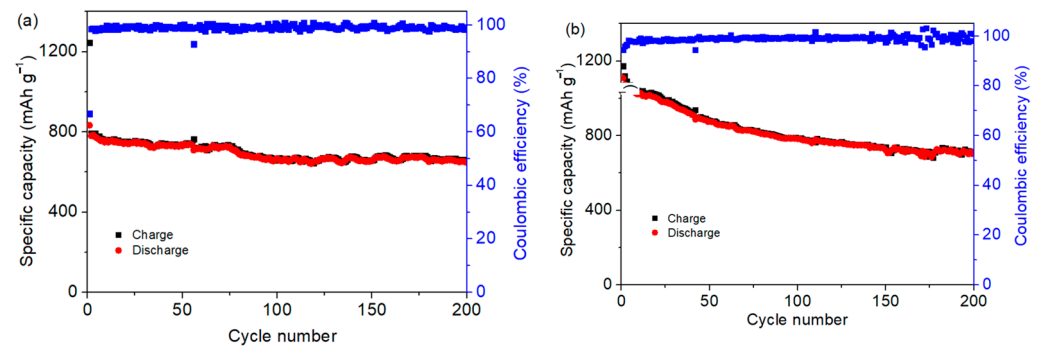


**Figure 8.** Specific capacities of  $\text{Co}_3\text{O}_4/\text{S}$ -infilled microcapsules when cycling at different temperatures of (a)  $-10\text{ }^\circ\text{C}$  and (b)  $50\text{ }^\circ\text{C}$  at 0.5C.

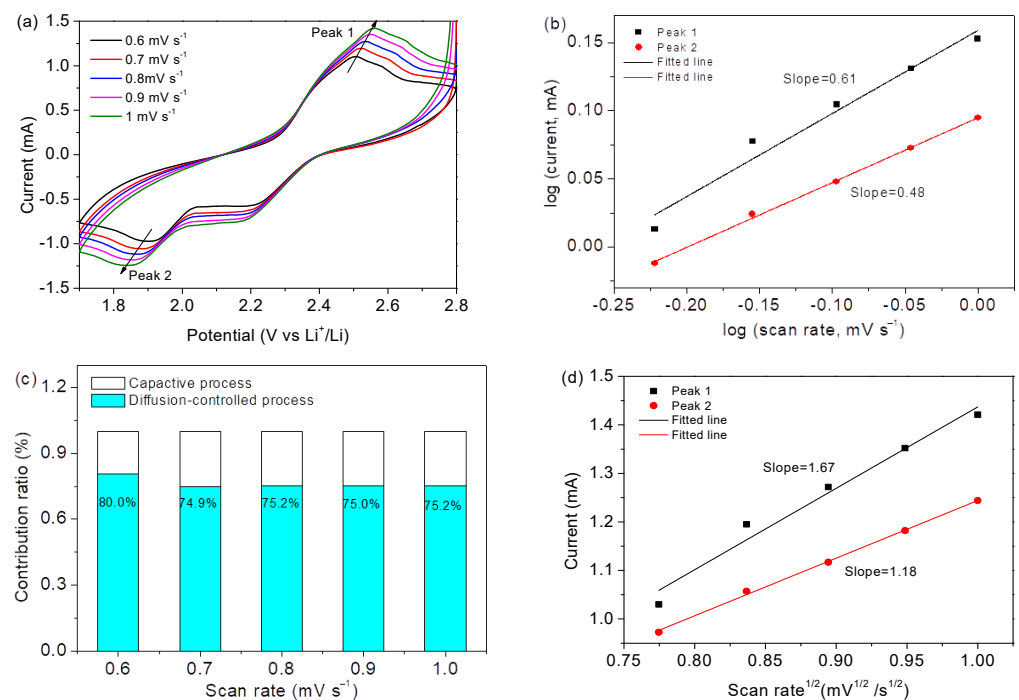


**Figure 9.** (a) CV profiles of the  $\text{Co}_3\text{O}_4/\text{S}$ -infilled microcapsules. (b) Relationship of  $\log(v)$  vs  $\log(i)$ . (c) Contribution ratios. (d) Relationship of peak current vs. rate.

### 2.3. DFT Calculations

The binding of the  $\text{Co}_3\text{O}_4$  with polysulfides was investigated by using DFT calculation on the adsorption energies. All calculations were conducted by using a Vienna Ab initio Simulation Package. In Figure 10, a series of surface adsorptions of  $\text{Co}_3\text{O}_4$  towards the polysulfides ( $\text{Li}_2\text{S}$ ,  $\text{Li}_2\text{S}_2$ ,  $\text{Li}_2\text{S}_4$ ,  $\text{Li}_2\text{S}_6$ ,  $\text{Li}_2\text{S}_8$ ) are presented. According to previous research [55–57], the (110) lattice plane in the  $\text{Co}_3\text{O}_4$  is more prone to exposure due to the presence of  $\text{Co}^{3+}$  on the surface. Therefore, we focused on the adsorption energy of the polysulfides on the  $\text{Co}_3\text{O}_4$  (110) surface. The side and top views of the geometric configurations of  $\text{Co}_3\text{O}_4$  (110) surface are shown in Figure 10a. Then, the adsorption models were built up for the calculation of adsorption energy, which is shown in Figure 11. Figure 10b shows the surface adsorption energies toward the polysulfides, where the surface adsorption energies of the  $\text{Co}_3\text{O}_4$  toward  $\text{Li}_2\text{S}$ ,  $\text{Li}_2\text{S}_2$ ,  $\text{Li}_2\text{S}_4$ ,  $\text{Li}_2\text{S}_6$ ,  $\text{Li}_2\text{S}_8$  are 3.8, 4.0, 1.7, 3.1, and 3.5 eV, respectively, indicating a good adsorption capability of  $\text{Co}_3\text{O}_4$  towards polysulfides. Figure 10c displays the charge density difference of the adsorption models. The distribution of the charge density connects polysulfides and  $\text{Co}_3\text{O}_4$ , indicating an electron transfer between

$\text{Co}_3\text{O}_4$  (110) surface and polysulfides. The charge density between polysulfides and  $\text{Co}_3\text{O}_4$  illustrates the formation of bonds and further verifies the adsorption stability.

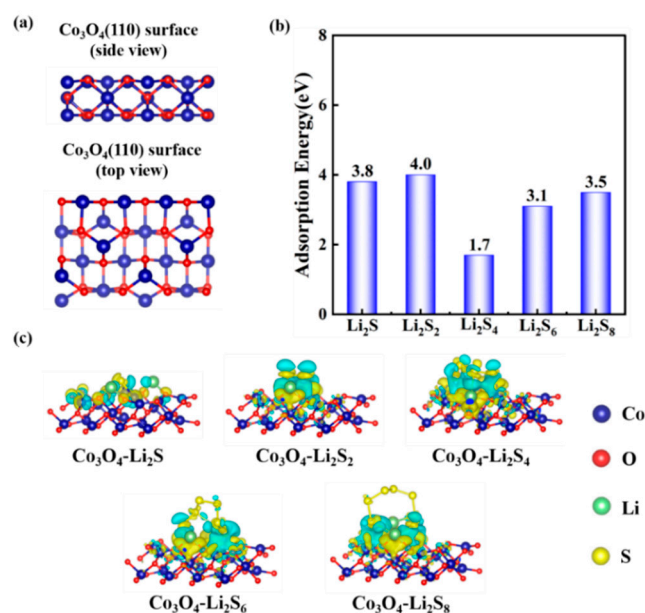


**Figure 10.** (a) Side and top views of the geometric configurations of  $\text{Co}_3\text{O}_4$  (110) surface. (b) Surface adsorption energies towards polysulfides. (c) Electron density differences of the polysulfides ( $\text{Li}_2\text{S}$ ,  $\text{Li}_2\text{S}_2$ ,  $\text{Li}_2\text{S}_4$ ,  $\text{Li}_2\text{S}_6$ ,  $\text{Li}_2\text{S}_8$ ).

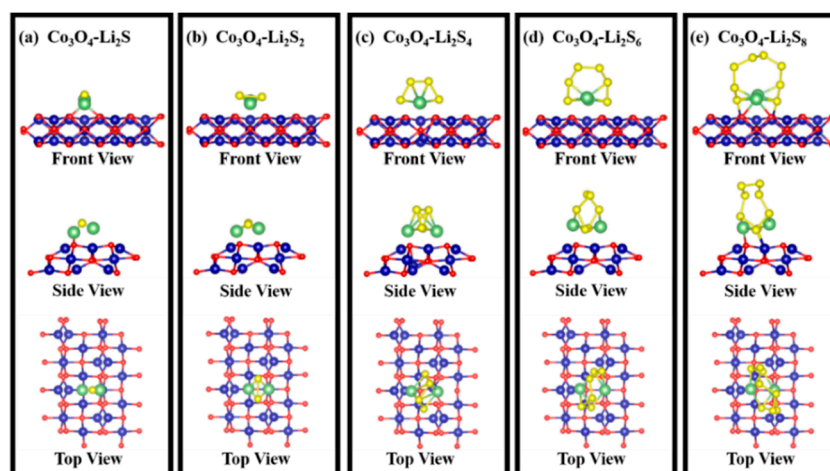


**Figure 11.** Adsorption models between polysulfides and  $\text{Co}_3\text{O}_4$  (110) surface: (a)  $\text{Co}_3\text{O}_4\text{-Li}_2\text{S}$ ; (b)  $\text{Co}_3\text{O}_4\text{-Li}_2\text{S}_2$ ; (c)  $\text{Co}_3\text{O}_4\text{-Li}_2\text{S}_4$ ; (d)  $\text{Co}_3\text{O}_4\text{-Li}_2\text{S}_6$ ; (e)  $\text{Co}_3\text{O}_4\text{-Li}_2\text{S}_8$ .

### 3. Conclusions

In summary, a novel microcapsule system encapsulated with MOFs-derived  $\text{Co}_3\text{O}_4/\text{S}$  nanocages is developed, which displays a good electrochemical performance as a Li-S battery cathode. Dodecahedral ZIF-67 was synthesized, then it was converted to a porous  $\text{Co}_3\text{O}_4$  nanocage which was infilled into a microcapsule through a microfluidic strategy. After 200 cycles at 0.5C, the specific capacity of  $\text{Co}_3\text{O}_4/\text{S}$ -infilled microcapsules remains  $935 \text{ mAh g}^{-1}$ . The Coulombic efficiency is about 100%. The constructed battery also shows a stable rate-performance, while good capacities are also achieved under both high and low temperatures of  $50 \text{ }^\circ\text{C}$  and  $-10 \text{ }^\circ\text{C}$ . In addition, DFT calculations verify that the  $\text{Co}_3\text{O}_4$  displays large binding energies towards all polysulfides including  $\text{Li}_2\text{S}$ ,  $\text{Li}_2\text{S}_2$ ,  $\text{Li}_2\text{S}_4$ ,  $\text{Li}_2\text{S}_6$ , and  $\text{Li}_2\text{S}_8$ , reducing the loss of polysulfides. It is expected that the developed

microcapsule system and the high performance will be applicable for engineering other emerging Li-storage nanomaterials.

**Supplementary Materials:** The following supporting information can be downloaded at: <https://www.mdpi.com/article/10.3390/nano12020236/s1>, Figure S1: (a) HRTEM image and (b) selective area electron diffraction (SAED) pattern of the porous  $\text{Co}_3\text{O}_4$ . Movie S1: Real-time process of the cone. Movie S2: Formation of drops.

**Author Contributions:** Conceptualization, J.L. (Jinyun Liu); methodology, J.L. (Jinyun Liu); software, J.C. and J.L. (Jinjin Li); validation, Y.Z. (Yajun Zhu), Y.Z. (Yan Zhong) and T.H.; formal analysis, J.L. (Jinyun Liu), Y.Z. (Yan Zhong) and Z.C.; investigation, Y.Z. (Yajun Zhu); resources, J.C. and Z.C.; data curation, Y.Z. (Yan Zhong); writing—original draft preparation, J.L. (Jinyun Liu) and Y.Z. (Yajun Zhu); writing—review and editing, J.L. (Jinyun Liu), Z.C. and J.L. (Jinjin Li); visualization, Y.Z. (Yan Zhong); supervision, J.L. (Jinyun Liu) and J.L. (Jinjin Li); project administration, J.L. (Jinyun Liu); funding acquisition, J.L. (Jinyun Liu) and J.L. (Jinjin Li). All authors have read and agreed to the published version of the manuscript.

**Funding:** This research was funded by Key Research and Development Program of Wuhu, grant number 2019YF07; Natural Science Research Project for Universities in Anhui Province, grant numbers KJ2018ZD034 and KJ2019A0502; National Key R&D Program of China, grant number 2021YFC2100100, National Natural Science Foundation of China, grant number 21901157, Shanghai Science and Technology Project of China, grant number 21JC1403400, University Synergy Innovation Program of Anhui Province, grant number GXXT-2020-073; and Foundation of Anhui Laboratory of Molecule-Based Materials, grant number FZJ21012. The APC was funded by Natural Science Research Project for Universities in Anhui Province.

**Institutional Review Board Statement:** Not applicable.

**Informed Consent Statement:** Not applicable.

**Data Availability Statement:** Data sharing not applicable.

**Conflicts of Interest:** The authors declare no conflict of interest.

## References

1. Yang, J.; Wang, J.; Dong, X.; Zhu, L.; Hou, D.; Zeng, W.; Wang, J. The potential application of  $\text{VS}_2$  as an electrode material for Mg ion battery: A DFT study. *Appl. Surf. Sci.* **2021**, *544*, 148775. [[CrossRef](#)]
2. Bella, F.; De Luca, S.; Fagiolari, L.; Versaci, D.; Amici, J.; Francia, C.; Bodoardo, S. An overview on anodes for magnesium batteries: Challenges towards a promising storage solution for renewables. *Nanomaterials* **2021**, *11*, 810. [[CrossRef](#)]
3. Narumoto, N.; Okamoto, N.; Saito, T. Surface structure control and charge/discharge characteristics of bismuth anode materials by electrodeposition for magnesium-ion batteries. *J. Mater. Sci.* **2021**, *32*, 9990–9997.
4. Shah, R.; Mittal, V.; Matsil, E.; Rosenkranz, A. Magnesium-ion batteries for electric vehicles: Current trends and future perspectives. *Adv. Mech. Eng.* **2021**, *13*, 16878140211003398. [[CrossRef](#)]
5. Zhang, X.; Xie, H.; Kim, C.; Zaghbi, K.; Mauger, A.; Julien, C. Advances in lithium-sulfur batteries. *Sci. Eng. R* **2017**, *121*, 1–29. [[CrossRef](#)]
6. Zhang, W.; Li, Y.; Lv, T.; Liu, W.; Luo, Y.; Guo, R.; Pei, H.; Lai, C.; Xie, J.  $\text{Ti}_3\text{C}_2/\text{CNTs}$  Macroporous conductive network boosts  $\text{Li}_4\text{Ti}_5\text{O}_{12}\text{-TiO}_2$  anode performance for practical Li ion and Mg ion batteries. *J. Electrochem. Soc.* **2021**, *168*, 030505. [[CrossRef](#)]
7. Lin, X.; Liu, J.; Zhang, H.; Zhong, Y.; Zhu, M.; Zhou, T.; Qiao, X.; Zhang, H.; Han, T.; Li, J. General liquid-driven coaxial flow focusing preparation of novel microcapsules for rechargeable magnesium batteries. *Adv. Sci.* **2021**, *8*, 2002298. [[CrossRef](#)]
8. Zuo, C.; Tang, W.; Lan, B.; Xiong, F.; Tang, H.; Dong, S.; Zhang, W.; Tang, C.; Li, J.; Ruan, Y.; et al. Unexpected discovery of magnesium-vanadium spinel oxide containing extractable  $\text{Mg}^{2+}$  as a high-capacity cathode material for magnesium ion batteries. *Chem. Eng. J.* **2021**, *405*, 127005. [[CrossRef](#)]
9. Du, C.; Younas, W.; Wang, Z.; Yang, X.; Meng, E.; Wang, L.; Huang, J.; Ma, X.; Zhu, Y.; Cao, C. Constructing sheet-assembled hollow CuSe nanocubes to boost the rate capability of rechargeable magnesium batteries. *J. Mater. Chem. A* **2021**, *9*, 3648–3656. [[CrossRef](#)]
10. Xue, X.; Chen, R.; Song, X.; Tao, A.; Yan, W.; Kong, W.; Jin, Z. Electrochemical  $\text{Mg}^{2+}$  displacement driven reversible copper extrusion/intrusion reactions for high-rate rechargeable magnesium batteries. *Adv. Funct. Mater.* **2021**, *31*, 2009394. [[CrossRef](#)]
11. Shen, K.; Zhang, Z.; Wang, S.; Ru, Q.; Zhao, L.; Sun, L.; Hou, X.; Chen, F. Cucumber-shaped construction combining bismuth nanoparticles with carbon nanofiber networks as a binder-free and freestanding anode for Li-ion batteries. *Energy Fuels* **2020**, *34*, 8987–8992. [[CrossRef](#)]

12. Tao, X.; Zhang, J.; Xia, Y.; Huang, H.; Du, J.; Xiao, H.; Zhang, W.; Gan, Y. Bio-inspired fabrication of carbon nanotiles for high performance cathode of Li-S batteries. *J. Mater. Chem. A* **2014**, *2*, 2290–2296. [[CrossRef](#)]
13. Zuo, C.; Xiao, Y.; Pan, X.; Xiong, F.; Zhang, W.; Long, J.; Dong, S.; An, Q.; Luo, P. Organic-inorganic superlattices of vanadium oxide@polyaniline for high-performance magnesium-ion batteries. *ChemSusChem* **2021**, *14*, 2093–2099. [[CrossRef](#)]
14. Sopha, H.; Tesfaye, A.T.; Zazpe, R.; Michalicka, J.; Dvorak, F.; Hromadko, L.; Krbal, M.; Prikryl, J.; Djenizian, T.; Macak, J.M. ALD growth of MoS<sub>2</sub> nanosheets on TiO<sub>2</sub> nanotube supports. *FlatChem* **2019**, *17*, 100130. [[CrossRef](#)]
15. Panwar, V.; Jain, S.L. Ternary hybrid TiO<sub>2</sub>-PANI-AuNPs for photocatalytic A<sub>3</sub>-coupling of aldehydes, amines and alkynes: First photochemical synthesis of propargyl amines. *Mater. Sci. Eng. C* **2019**, *99*, 191–201. [[CrossRef](#)] [[PubMed](#)]
16. Wang, S.; Liu, F.; Gao, C.; Wan, T.; Wang, L.; Wang, L.; Wang, L. Enhancement of the thermoelectric property of nanostructured polyaniline/carbon nanotube composites by introducing pyrrole unit onto polyaniline backbone via a sustainable method. *Chem. Eng. J.* **2019**, *370*, 322–329. [[CrossRef](#)]
17. Chen, Y.; Ji, X. Bamboo-like Co<sub>3</sub>O<sub>4</sub> nanofiber as host materials for enhanced lithium-sulfur battery performance. *J. Alloys Compd.* **2019**, *777*, 688–692. [[CrossRef](#)]
18. Bosubabu, D.; Sivaraj, J.; Gurunathan, P.; Ramesha, K. Hollow Co<sub>3</sub>O<sub>4</sub> microspheres grafted with nitrogen-doped carbon nanotubes as efficient sulfur host for high performing lithium-sulfur batteries. *Energy Fuels* **2020**, *34*, 16810–16818. [[CrossRef](#)]
19. Wang, P.; Zeng, R.; You, L.; Tang, H.; Zhong, J.; Wang, S.; Yang, T. Graphene-like matrix composites with Fe<sub>2</sub>O<sub>3</sub> and Co<sub>3</sub>O<sub>4</sub> as cathode materials for lithium-sulfur batteries. *ACS Appl. Nano Mater.* **2020**, *3*, 1382–1390. [[CrossRef](#)]
20. Saroha, R.; Oh, J.H.; Lee, J.S.; Kang, Y.C.; Jeong, S.M.; Kang, D.W.; Cho, C.; Cho, J.S. Hierarchically porous nanofibers comprising multiple core-shell Co<sub>3</sub>O<sub>4</sub>@graphitic carbon nanoparticles grafted within N-doped CNTs as functional interlayers for excellent Li-S batteries. *Chem. Eng. J.* **2021**, *426*, 130805. [[CrossRef](#)]
21. Wang, S.; Hou, X.; Zhong, Z.; Shen, K.; Zhang, G.; Yao, L.; Chen, F. Co<sub>3</sub>O<sub>4</sub>-NP embedded mesoporous carbon rod with enhanced electrocatalytic conversion in lithium-sulfur battery. *Sci. Rep.* **2018**, *8*, 16133. [[CrossRef](#)]
22. Xu, J.; Su, D.; Wang, G. Co<sub>3</sub>O<sub>4</sub>-carbon cloth free standing cathode for lithium sulfur battery. *IOP Conf. Ser. Mater. Sci. Eng.* **2017**, *222*, 012013. [[CrossRef](#)]
23. Cheng, H.; Wang, S.; Tao, D.; Wang, M. Sulfur/Co<sub>3</sub>O<sub>4</sub> nanotube composite with high performances as cathode materials for lithium sulfur batteries. *Funct. Mater. Lett.* **2014**, *7*, 1450020. [[CrossRef](#)]
24. Zhang, K.; Xu, Y.; Lu, Y.; Zhu, Y.; Qian, Y.; Wang, D.; Zhou, J.; Lin, N.; Qian, Y. A graphene oxide-wrapped bipyramidal sulfur@polyaniline core-shell structure as a cathode for Li-S batteries with enhanced electrochemical performance. *J. Mater. Chem. A* **2016**, *4*, 6404–6410. [[CrossRef](#)]
25. Ali, M.; Guzman, R.C.; Cojocari, O.; Nellen, S.; Santamaría, G.; García-Munoz, L.E.; Segovia-Vargas, D.; Globisch, B.; Carpintero, G. Quasi-optic transmitter and receiver modules enabling next-Generation ultra-broadband wireless links at carrier-wave frequencies ranging from 60 to 180 GHz. *J. Infrared Millim. Terahertz Waves* **2019**, *40*, 688–695. [[CrossRef](#)]
26. Lv, C.; Li, S.; Che, Y.; Chen, H.; Shu, Y.; He, J.; Song, J. Study on the molybdenum electro-extraction from MoS<sub>2</sub> in the molten salt. *Sep. Purif. Technol.* **2021**, *258*, 118048. [[CrossRef](#)]
27. Tian, Y.; Zhou, M.; Pan, Y.; Du, X.; Wang, Q. MoS<sub>2</sub> as highly efficient co-catalyst enhancing the performance of Fe<sup>0</sup> based electro-fenton process in degradation of sulfamethazine: Approach and mechanism. *Chem. Eng. J.* **2021**, *403*, 126361. [[CrossRef](#)]
28. Wang, Z.; Zhang, J.; Wen, T.; Liu, X.; Wang, Y.; Yang, H.; Sun, J.; Feng, J.; Dong, S.; Sun, J. Highly effective remediation of Pb(II) and Hg(II) contaminated wastewater and soil by flower-like magnetic MoS<sub>2</sub> nanohybrid. *Sci. Total Environ.* **2020**, *699*, 134341. [[CrossRef](#)] [[PubMed](#)]
29. Wu, J.C.; Chen, S.S.; Yu, T.-C.; Wu, K.C.W.; Hou, C.H. Effective electrochemically controlled removal of fluoride ions using electrodeposited polyaniline-carbon nanotube composite electrodes. *Sep. Purif. Technol.* **2021**, *254*, 117561. [[CrossRef](#)]
30. Huang, Z.; Shi, L.; Muhammad, Y.; Li, L. Effect of ionic liquid assisted hydrothermal carbonization on the properties and gasification reactivity of hydrochar derived from eucalyptus. *J. Colloid Interface Sci.* **2021**, *586*, 423–432. [[CrossRef](#)]
31. Xu, K.; Liao, N.; Zhang, M.; Xue, W. Atomic-scale investigation of enhanced lithium, sodium and magnesium storage performance from defects in MoS<sub>2</sub>/graphene heterostructures. *Nanoscale* **2020**, *12*, 7098–7108. [[CrossRef](#)] [[PubMed](#)]
32. Parra-Arciniega, S.M.; González-Juárez, E.; Hernández-Carrillo, R.A.; Briones-Martínez, R.; Jiménez-Barrera, R.M.; García-Gómez, N.A.; Sánchez, E.M. A Mg<sup>2+</sup>/Li<sup>+</sup> hybrid-ion battery based on MoS<sub>2</sub> prepared by solvothermal synthesis with ionic liquid assistance. *J. Mater. Sci. Mater. Electron.* **2020**, *31*, 14702–14713. [[CrossRef](#)]
33. Cui, L.; Zhou, L.; Kang, Y.M.; An, Q. Recent advances in the rational design and synthesis of two-dimensional materials for multivalent ion batteries. *ChemSusChem* **2020**, *13*, 1071–1092. [[CrossRef](#)] [[PubMed](#)]
34. Duan, D.H.; Zhao, W.W.; Chen, K.X.; Wang, Y.F.; Liu, S.B.; Zhou, X.X.; Chen, L.; Li, Y. MOF-71 derived layered Co-CoP/C for advanced Li-S batteries. *J. Alloy. Compd.* **2021**, *886*, 161203. [[CrossRef](#)]
35. Pu, X.; Song, T.; Tang, L.; Tao, Y.; Cao, T.; Xu, Q.; Liu, H.; Wang, Y.; Xia, Y. Rose-like vanadium disulfide coated by hydrophilic hydroxyvanadium oxide with improved electrochemical performance as cathode material for aqueous zinc-ion batteries. *J. Power Sources* **2019**, *437*, 226917. [[CrossRef](#)]
36. Sihag, A.; Xie, Z.L.; Thang, H.V.; Kuo, C.L.; Tseng, F.G.; Dyer, M.S.; Chen, H.Y.T. DFT Insights into Comparative Hydrogen Adsorption and Hydrogen Spillover Mechanisms of Pt<sub>4</sub>/Graphene and Pt<sub>4</sub>/Anatase (101) Surfaces. *J. Phys. Chem. C* **2019**, *123*, 25618–25627. [[CrossRef](#)]

37. Li, Y.; Xu, D.; Zhang, D.; Wei, Y.; Zhang, R.; Guo, Y. Study on MnO<sub>2</sub>/MXene–Ti<sub>3</sub>C<sub>2</sub> composite materials as cathode materials for magnesium batteries. *RSC Adv.* **2019**, *9*, 33572–33577. [[CrossRef](#)]
38. Liu, Z.; Liu, B.; Guo, P.; Shang, X.; Lv, M.; Liu, D.; He, D. Enhanced electrochemical kinetics in lithium-sulfur batteries by using carbon nanofibers/manganese dioxide composite as a bifunctional coating on sulfur cathode. *Electrochim. Acta* **2018**, *28*, 180–187. [[CrossRef](#)]
39. Li, X.; Ma, Y.; Tang, C. Advanced Co<sub>3</sub>O<sub>4</sub> interlayer as an efficient polysulfide barrier for high-performance Li-S batteries. *Int. J. Electrochem. Sci.* **2019**, *14*, 3245–3252.
40. Wang, J.; Xiao, K.; Ouyang, B.; Zhang, L.; Yang, H. Simultaneous immobilization and conversion of polysulfides on Co<sub>3</sub>O<sub>4</sub>-CoN heterostructured mediators toward high-performance lithium-sulfur batteries. *ACS Appl. Energy Mater.* **2019**, *2*, 2570–2578. [[CrossRef](#)]
41. Mussa, Y.; Arsalan, M.; Alsharaeh, E. Cobalt oxide/graphene nanosheets/hexagonal boron nitride (Co<sub>3</sub>O<sub>4</sub>/CoO/GNS/h-BN) catalyst for high sulfur utilization in Li–S batteries at elevated temperatures. *Energy Fuels* **2021**, *35*, 8365–8377. [[CrossRef](#)]
42. Zhou, L.; Li, H.; Wu, X.; Zhang, Y.; Danilov, D.; Eichel, R.; Notten, P. Double-shelled Co<sub>3</sub>O<sub>4</sub>/C nanocages enabling polysulfides adsorption for high-performance lithium-sulfur batteries. *ACS Appl. Energy Mater.* **2019**, *2*, 8153–8162. [[CrossRef](#)]
43. Li, Y.; Yao, C.; Wang, C.; Yang, P.; Wu, R.; Fei, L.; Zhang, Y.; Jiang, Y. An approach through steam to form sulfur nanoparticles for lithium sulfur batteries. *Electrochim. Commun.* **2021**, *125*, 107010. [[CrossRef](#)]
44. Liu, B.; Huang, S.; Kong, D.; Hu, J.; Yang, H. Bifunctional NiCo<sub>2</sub>S<sub>4</sub> catalysts supported on a carbon textile interlayer for ultra-stable Li-S battery. *J. Mater. Chem. A* **2019**, *7*, 7604. [[CrossRef](#)]
45. Zeng, P.; Chen, M.; Luo, J.; Liu, H.; Li, Y.; Peng, J.; Li, J.; Yu, H. Carbon-coated yttria hollow spheres as both sulfur immobilizer and catalyst of polysulfides conversion in lithium-sulfur batteries. *ACS Appl. Mater. Interfaces* **2019**, *11*, 42104–42113. [[CrossRef](#)]
46. Liu, Y.; Chatterjee, A.; Rusch, P.; Wu, C.; Nan, P.; Peng, M. Monodisperse Molybdenum Nanoparticles as Highly Efficient Electrocatalysts for Li-S Batteries. *ACS Nano* **2021**, *15*, 15047–15056. [[CrossRef](#)]
47. Sun, D.; Zhou, J.; Rao, D.; Zhu, L.; Niu, S.; Cai, J.; Fang, Y. Regulating the electron filling state of d orbitals in Ta-based compounds for tunable lithium-sulfur chemistry. *Sustain Mater. Technol.* **2021**, *28*, e00271. [[CrossRef](#)]
48. Zhou, P.; Han, T.; Gu, C.; Li, J.; Shen, Z.; Zhang, H.; Niu, J. A novel wheel-confined composite as cathode in Li-S batteries with high capacity retention. *J. Alloy Compd.* **2019**, *776*, 504–510. [[CrossRef](#)]
49. Du, C.; Zhu, Y.; Wang, Z.; Wang, L.; Younas, W.; Ma, X.; Cao, C. Cuprous self-doping regulated mesoporous CuS nanotube cathode materials for rechargeable magnesium batteries. *ACS Appl. Mater. Interfaces* **2020**, *12*, 35035–35042. [[CrossRef](#)] [[PubMed](#)]
50. Zhang, Y.; Liu, G.; Zhang, C.; Chi, Q.; Zhang, T.; Feng, Y.; Zhu, K.; Zhang, Y.; Chen, Q.; Cao, D. Low-cost MgFe<sub>x</sub>Mn<sub>2-x</sub>O<sub>4</sub> cathode materials for high-performance aqueous rechargeable magnesium-ion batteries. *Chem. Eng. J.* **2020**, *392*, 123652. [[CrossRef](#)]
51. Tao, X.; Wang, J.; Liu, C.; Wang, H.; Yao, H.; Zheng, G.; Seh, Z.; Cai, Q.; Li, W.; Zhou, G.; et al. Balancing surface adsorption and diffusion of lithium polysulfides on nonconductive oxides for lithium-sulfur battery design. *Nat. Commun.* **2016**, *7*, 11203. [[CrossRef](#)]
52. Zhu, P.; Zhu, J.; Zang, J.; Chen, C.; Lu, Y.; Jiang, M.; Yan, C.; Dirican, M.; Selvan, R.; Zhang, X. A novel bi-functional double-layer rGO-PVDF/PVDF composite nanofiber membrane separator with enhanced thermal stability and effective polysulfide inhibition for high-performance lithium-sulfur batteries. *J. Mater. Chem. A* **2017**, *5*, 15096–15104. [[CrossRef](#)]
53. Gao, G.; Zheng, F.; Wang, L. Solid 3D Li–S battery design via stacking 2D conductive microporous coordination polymers and amorphous Li–S layers. *Chem. Mater.* **2020**, *32*, 1974–1982. [[CrossRef](#)]
54. Wang, K.; Guan, Y.; Jin, Z.; Wang, W.; Wang, A. Te<sub>0.045</sub>S<sub>0.955</sub> PAN composite with high average discharge voltage for Li-S battery. *J. Energy Chem.* **2019**, *39*, 249–255. [[CrossRef](#)]
55. Zhang, H.; Cao, D.; Bai, X. Ni-Doped magnesium manganese oxide as a cathode and its application in aqueous magnesium-ion batteries with high rate performance. *Inorg. Chem. Front.* **2020**, *7*, 2168–2177. [[CrossRef](#)]
56. Harudin, N.; Osman, Z.; Majid, S.R.; Othman, L.; Hambali, D.; Silva, M.M. Improved electrochemical properties of MgMn<sub>2</sub>O<sub>4</sub> cathode materials by Sr doping for Mg ion cells. *Ionics* **2020**, *26*, 3947–3958. [[CrossRef](#)]
57. Asif, M.; Rashad, M.; Shah, J.H.; Zaidi, S.D.A. Surface modification of tin oxide through reduced graphene oxide as a highly efficient cathode material for magnesium-ion batteries. *J. Colloid Interface Sci.* **2020**, *561*, 818–828. [[CrossRef](#)]